Research Article

Enhancement of photocatalytic by Mn_3O_4 spinel ferrite decorated graphene oxide nanocomposites

Tanawat Imboon[1] · Jeerawan Khumphon[1] · Khrongkhwan Yotkuna[1] · I-Ming Tang[2] · Sirikanjana Thongmee[1]

Received: 10 February 2021 / Accepted: 5 May 2021
Published online: 22 May 2021

Abstract
The hydrothermal process was used to prepare Mn_3O_4/x%GO nanocomposites (NC's) having different ratios of the Mn_3O_4 nanoparticles (NP's) on the surface of graphene oxide (GO) sheet. SEM image showed that the Mn_3O_4 NP's were distributed over the surface of GO sheet. HRTEM images exhibited the lattice fringe arising from the (101) plane of the Mn_3O_4 NP's having the interplanar d-spacing of 0.49 nm decorating on the surface of GO. The electronic absorption spectra of Mn_3O_4/x%GO NC's also show broad bands from 250 to 550 nm. These bands arise from the d–d crystal field transitions of the tetrahedral Mn^{3+} species and indicate a distortion in the crystal structure. Photo-catalytic activity of spinel ferrite Mn_3O_4 NP's by themselves was low but photo-catalytic activity is enhanced when the NP's are decorating the GO sheet. Moreover, the Mn_3O_4/10%GO NC's showed the best photo-catalytic activity. This result comes from the formation of Mn–O–C bond that confirm by FT-IR. This bond would facilitate the transfer of the photoelectrons from the surfaces of the NP's to the GO sheets. PL emission which is in the violet–red luminescent region shows the creation of defects in the fabricated Mn_3O_4 NP's nanostructures. These defects create the defect states to which electrons in the VB can be excited to when the CB. The best degradation efficiency was achieved by the Mn_3O_4 NP's when they were used to decorate the GO sheets in the Mn_3O_4/10%GO NC's solution.

Highlights

1. Lattice fringe of Mn3O4 with an interplanar d-spacing of 0.49 nm for (101) plane.
2. Photocatalytic activity of spinel ferrite Mn3O4 nanoparticles by itself is low.
3. Number of photoelectrons created depends on number of Mn3O4 on a given area of GO
4. The bonding of the Mn3O4 to the GO sheet would be though a Mn–O–C junction.
5. The degradation processes were accelerated by Mn3O4/10%GO nanocomposites

✉ Sirikanjana Thongmee, fscisjn@ku.ac.th | [1]Department of Physics, Faculty of Science, Kasetsart University, Bangkok 10900, Thailand. [2]Department of Physics, Faculty of Science, Mahidol University, Bangkok 10400, Thailand.

Graphic abstract

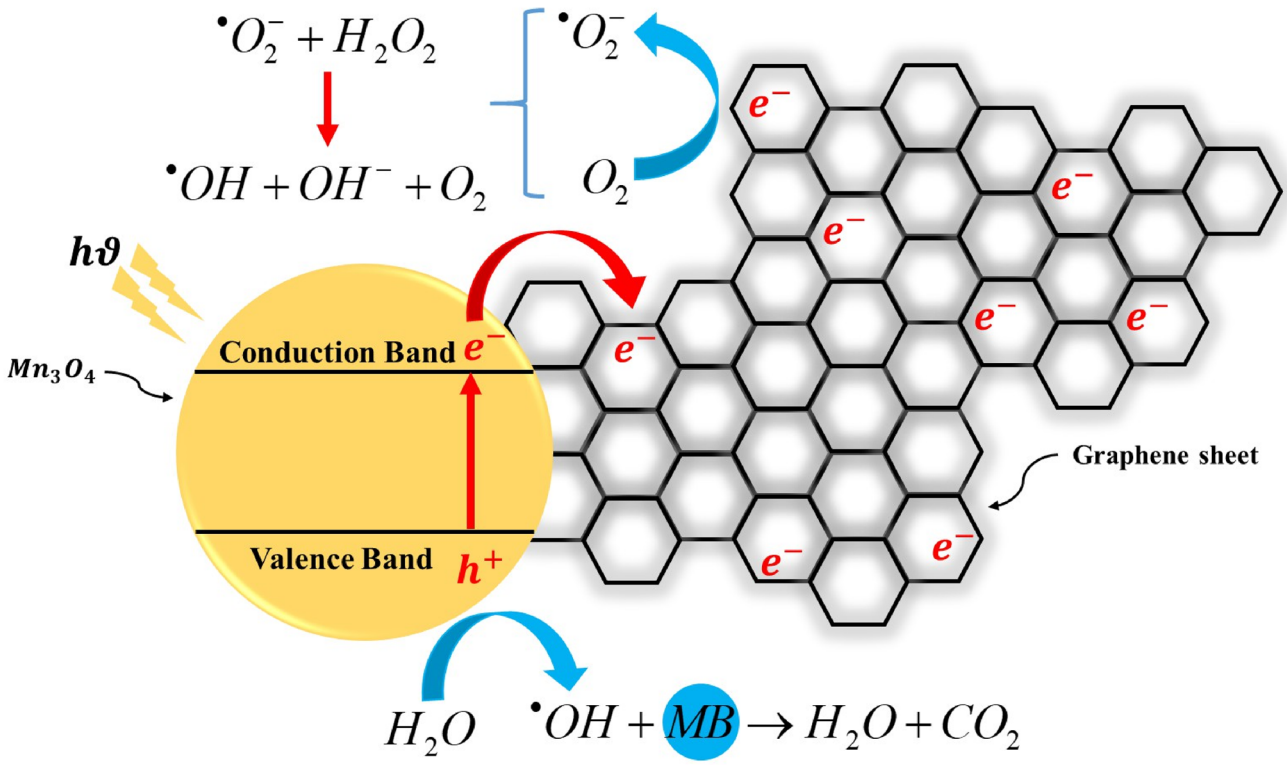

Mechanism of a Mn_3O_4/x%GO nanocomposites for photocatalytic activity

Keywords GO sheet · Mn_3O_4 NP's · Mn_3O_4/x%GO NC's · Photo-catalytic activity · Photoluminescence spectra · Nanoparticles

1 Introduction

In recent years, many researchers are interested in graphene and graphene based materials due to its excellent physical and chemical properties such as high electron conductivity, unique transport performance [1], high mechanical strength [2], extremely high specific surface area [3] and easy functionalization make graphene a good substrate to produce graphene-based composites. Graphene is an allotrope of carbon with two-dimensional honeycomb sp^2 crystalline lattice. Also, it has been considered as the thinnest and hardest material. Due to these properties graphene has been extensively explored and utilized for the alteration of hydrogen storage [4], supercapacitor [5–8], energy storage [9–11], biosensors [12], electrocatalyst [13–16] and photocatalysts [17–19]. In addition, there are various methods used to synthesis of graphene based materials such as arc discharge method [20–22], laser based technique [23], microwave irradiation [24], microwave assisted materials [25–27], spray pyrolysis [28] and hydrothermal method [17, 18]. Recently, a few novel methods have been reported. Kumar et al. [29] have been synthesized the ternary hybrids material containing manganese cobaltite (MnCo2O4) nanoparticles wrapped by microwave exfoliated-reduced graphene oxide nanosheets (ME-rGO NSs) for improved supercapacitor electrode materials. Choucair et al. [30] have shown a method to prepare graphene based on hydrothermal synthesis and sonication. The recent advances in the large-scale synthesis of graphene by CVD on TiO_2 [31] and Cu [32] films open up various macroscopic applications of graphene. In addition, graphene have been led to investigate the design and the development low-cost and high yield preparation protocols for chemically-derived

graphene (graphene oxide). Graphene oxide (GO) has received increasing the attention. This is because it possesses similar properties to that of graphene. The structure also consists of polar functional groups i.e. hydroxyl, carboxyl, etc. on its planar surface that will have high surface area, thermal stability, mechanical and electrical properties. Therefore, GO can be used to combine with metal oxide nanomaterials for photocatalytic activity [33–36]. A graphene layer interfacing with the distribution of nanoparticles (NPs) on the surface have been well defined. The NPs can act as a stabilizer against the aggregation of individual graphene sheets, which is generally caused by a strong Van der Waals interaction between graphene layers. Some researchers reported on the modification of graphene with metal oxide NPs such as TiO_2, SnO_2, and Fe_2O_3 [37–39]. The incorporation of nanoparticles on the surface of graphene is highly desirable for improving the surface morphology for example: electronic structure and following intrinsic properties of graphene. Generally, various types of metal oxides have been synthesized and supported on graphene, which include ZnO, TiO_2, CeO_2, SnO_2, MnO_2, Co_3O_4, Fe_3O_4, WO_3 [40, 41]. In case of TiO_2 and ZnO, they exhibited good photocatalytic activity in UV light because of their wide band gap and they are stable in aqueous conditions during photocatalysis. Furthermore, the coupling of graphene oxide with TiO_2 and ZnO increases the photocatalytic activity due to increase in the photogenerated charge carriers. The photocatalytic efficiency depends on the ratio of the photogenerated charge-carrier transfer rate to the rate of electron-hole recombination. For composite structure, M^{2+} ion easily bonds with oxygen by giving an electron and super oxide radical. For NP's, when the photoelectron meets a radical in the solution immersing the NP's, a photo-chemical reaction involving the radical could occur. During photo chemical degradation of metal oxide, it found that the photo will generate holes and will react the adsorbed molecules in the water to form OH radicals that can be oxidized the organic compounds [42]. In case of waste water treatment, people use TiO_2, ZnO and spinel ferrite (Mn_3O_4) NP's. This is because of the environmental friendly. As we know, ZnO is the semiconductor. The photoelectrons can excite into the conduction band and they will interact with the holes that left behind in the valence band to form an e^-/h^+ pair which called an exciton. When these two recombination, there will be an exciton emission close to the Near Band Edge (NBE). The nanoparticles which formed the excitons will have poor photo-catalytic performances. This is because the photoelectrons that created by the absorption of the light will not be available for the photo-catalytic activity. In case of the trimanganese tetraoxide (Mn_3O_4) NP's, it has an excellent potential such as its ability to adapt to the different oxidation states which are needed for many applications in the photo-catalysis and in the solar energy conversion [43, 44]. Moreover, Mn_3O_4 has a distorted spinel structure, a unique ion exchange and a special electronic configuration. [45, 46] The first excited states of the Mn^{3+} ion will stay in the band gap of the host which will lead to a luminescence needed for certain photo-catalytic applications [47]. Therefore, several researchers have been recognized as an important photocatalyst that is highly effective in visible light. Table 1 shows the summary some of the results that have been obtained till date with Mn_3O_4 as photocatalytic nanomaterials. Mn_3O_4 can be

Table 1 Summary of photocatalytic performance of Mn_3O_4 nanomaterials reported in recent papers till date

Catalyst	Method	Amount of catalyst	Dye molecule	Source of light	Time for degradation (min)	%Degradation	References
Mn_3O_4 micro-dandelions	Reflux	25 µg	Alizarin red2.0 µM	Tungsten lamp	120	50	Rahaman and Ghosh [55]
rGO/Mn_3O_4nano-composites	Reflux	10 mg	Methylene blue 12 mg L^{-1}	Sunlight irradiation	60	73–96 (Depending on the amount of Mn3O4 and rGO)	Ghosh et al. [56]
Mn_3O_4/GO composite	Hydrothermal	0.1 g	Methyl orange 20 mg L^{-1}	LED lamp	240	95	Osgoueiet al. [53]
rGO/Mn_3O_4	Hydrothermal	1 g	Methylene blue 10 mg L^{-1}	Hg lamp	240	21 (Mn3O4) 100 (rGO/Mn3O4)	Mousaet al. [54]
Mn_3O_4	Sol–gel	0.05 g	Congo red 30 mg L^{-1}	UV-visible-light irradiation	120	38	. Rizal et al. [57]
Mn_3O_4/x%GO	Hydrothermal	40 mg	Methylene Blue 10 mg L^{-1}	UV lamp	180	0.33–60 (Depending on the amount of GO)	Present work

used to oxidize the organic compounds for example: explosives, dyes, aromatic amines and mineralization that found in nature [48–52]. A lot of researchers have therefore focused on the synthesis and the study on the properties of Mn_3O_4 nanomaterials. Osgouei MS et al. [53] have synthesized vanadium doped and thallium doped Mn_3O_4 nanoparticles as well as Mn_3O_4/Cu nanorod hybrids by hydrothermal method. They found that the photocatalytic activity of the obtained samples were evaluated in removal of Methyl Orange (MO) under a visible light irradiation of 9 W LED lamp. Mousa MA et al. [54] used the hydrothermal method for synthesizing Mn_3O_4 nanoparticles and rGO-M nanocomposites and evaluating the photocatalytic efficiency using aqueous solution of MB under visible light irradiation. They found that rGO-Mn_3O_4 has shown higher photocatalytic efficiency than pure Mn_3O_4 under visible light illumination without any oxidants; while rGO shown complete adsorption of MB in dark. Rahaman H and Ghosh SK [55] described the synthesis of dandelion shaped Mn_3O_4 microstructures using dye/surfactant assemblies as soft-templates by reflux method. Moreover, Ghosh, Basu and Baskey [56] used the reflux condensation method to fabricate their Mn_3O_4 NP's. The result found thatMn_3O_4 nanomaterials were successfully applied to degrade the organic dyes in water but compared to Mn_3O_4 nanomaterials the rGO/ Mn_3O_4 nanocomposites are found to most heavily enhance the dye degradation efficiency under solar light irradiation due to large surface area of rGO surface. Rizal MY et al. [57] have been reported Mn_3O_4 was prepared via a conventional sol–gel method and the composites containing Ag were synthesized with various Ag–to–Mn_3O_4 molar ratios via a hydrothermal technique. The result of this work showed that a high-efficiency reaction under visible light and a substantial photocatalytic improvement under ultrasound. The degradation process was found to be optimal under strongly acidic conditions and the best Ag -to- Mn_3O_4 molar ratio was found to be 1:0.5. Kefeni and Mamba [58] reviewed the use of different spinel ferrite NP's. While Hu, Lu, Chen and Zhang [59] reviewed how the photo-catalytic of metal oxides can be improved when they are formed graphene-metal composites by using chemical vapor deposition (CVD) method. Recently, Ma et al. [60], have decorated the spinel ferrite Mn_3O_4 on reduced graphene oxide (rGO) to improve photo-catalytic performances. Yuqian Li et al. [61], described the efficiency of graphene oxide/Mn_3O_4 hybrids which have the perfect degradation of methylene blue. They found that as prepared graphene oxide/Mn_3O_4 led to the improvement of the reaction rate compared to Mn_3O_4 nanoparticles. Ahmed A. Amer et al. [62], showed that Mn_3O_4 GO NC's would have high microwave absorption and high photo-catalytic activity for the reduction of 1-naphthyl-amine. L. Duan et. al. [63], reported that the Mn_3O_4–rGO NC's also has high oxidation properties when compared to the Mn_3O_4 Chandra et al. [64], found that Mn_2O_3 NP's decorated rGO acted against several dynes such as eosin, methylene B and rhosanmine B within a few minutes. Atique Ullah et al. [65], reported that the Mn_3O_4 NP's need time about 240 min to degrade methylene blue (MB) while Mn_3O_4·rGO used time to degrade MB only 60 min. The differences indicate that the Mn_3O_4 nanoparticles alone are poor photo-catalyst. Furthermore, they found that the percentage of the degradation depended on the amounts of the NP's and the GO.In this work, we are interested in the decorating the graphene oxide (GO) with the Mn_3O_4 NP's by using hydrothermal method to make both the Mn_3O_4 NP's and the Mn_3O_4/x%GO NC's. We have determined the optical properties and photo-catalytic activity of the different Mn_3O_4/x%GO NC's (where x is the weight % of the GO in the composites). To do this, we have studies the reduction of MB by the photoelectrons generated when the Mn_3O_4 is exposed to the ultraviolet (UV) light. MB is the brightly colored blue cationic thiazine dye. Photo-catalytic activities can be determined by the disappearance of the blue color. The reduction of MB by the Mn_3O_4/x%GO NC's can be monitored by looking at the absorption lines centered at 614 nm and 660 nm.

Table 2 The amount of substance for preparation of Mn_3O_4/x%GO nanocomposites

Mn_3O_4/x%GO	Amount of substance (g)	
	Mn_3O_4	GO
x = 0	0.4000	0.0000
x = 5	0.4000	0.0211
x = 10	0.4000	0.0444
x = 15	0.4000	0.0706
x = 20	0.4000	0.1000

2 Experimental details

2.1 Synthesis of Mn_3O_4 nanoparticles

Mn_3O_4 nanoparticles were prepared by the hydrothermal process. This process is cost-effective and simple. It uses hot water and high vapor pressure. In the hydrothermal process, the reaction is a chemical process and the ions are able to come into contact with each other more easily. The higher room temperature used in the autoclave allows the oxide compounds to disassociate into their ion constitutes since the solubility increases with temperature. The high pressure is needed so that the solvent does not evaporate. At the high temperature (180 °C), the ions will move faster. After the nanoparticles are formed, the solution is cooled

down to room temperature. The solubility drops and the nanoparticles precipitate out [66] 3.9550 g of $KMnO_4$ was dissolved in 70 ml of deionized water while being stirred. Then, 13.2 ml of hydrazine hydrate (80% wt%) was added into the solution drop by drop. The mixture was constantly stirred for 30 min. After that the mixture was transferred to a Telfon-lined autoclave and was heated at 180 °C for 6 h to make the reaction of the mixture to be Mn_3O_4 nanoparticles. The precipitate of Mn_3O_4 nanoparticles was removed by filtration, washed with water and dried at 60 °C for overnight.

2.2 Synthesis of graphene oxide

Graphene oxide (GO) is prepared from graphite which can be used as promising starting material to generate graphene-based nanocomposites. The advantage of graphene oxide is cheaper and easier to manufacture than graphene and reduced graphene oxide. Moreover, graphene oxide can easily be mixed with different materials and polymers. It is also enhance the properties of composite materials such as tensile strength, conductivity and photocatalytic activity. Graphene oxide (GO) was synthesized using the modified Hummer's method [67] Firstly, 0.75 g of graphite flakes was mixed into 100 ml of H_2SO_4 while being stirred for 30 min while in an ice bath. The temperature of the mixture was held below 5 °C. Then, 4.5 g of $KMnO_4$ and 0.31 g of $NaNO_3$ were added into the solution slowly for oxidizing functional group. The mixture was stirred in an ice bath for 30 min. Then, the mixture was removed from the ice bath and further stirred continuously at room temperature for 120 h. After stirred for 120 h, an aqueous 100 ml of deionized water was added into the mixture. After that the mixture was heated at 98 °C for 1 h. Then, 7.5 ml of H_2O_2 solution was added into the mixture to stop the reaction. At this point, 50 ml of HCl, 50 ml of deionized water and 50 ml of ethanol were added to the mixture for removing the oxidance from the reaction. The black precipitates were washed with the mixture of 5% HCl and deionized water for several times until the filtrated solution reached a pH of 7. The solution was then centrifuged to remove the GO powder. The GO powders were dried using freeze dehydration at – 40 °C to obtain the GO.

2.3 Synthesis of the Mn_3O_4/x% GO nanocomposites

The Mn_3O_4/x% GO NC's was fabricated using the hydrothermal method. A fixed amount of the Mn_3O_4 NP's and different amounts of GO were used to fabricated the Mn_3O_4·x% GO NC's (with x = 0, 5, 10, 15 and 20 wt%) as shown in Table 2. After the different amounts of the GO were weighted out, they were dispersed into 80 ml of deionized water in an ultrasonic bath for 3 h to form GO sheets, individually. Then, 0.4 g of Mn_3O_4 nanoparticles was added into the GO solution and stirred for 1 h. This means that the coverage of the GO sheets by the Mn_3O_4 nanoparticles decreased as x increased. The different mixtures were separately transferred to the Teflon-lined autoclave which was heated at 180 °C for 6 h for making the reaction of the Mn_3O_4/x% GO nanocomposites. The precipitates of Mn_3O_4/x% GO nanocomposites were filtered out and washed with deionized water. All the samples were

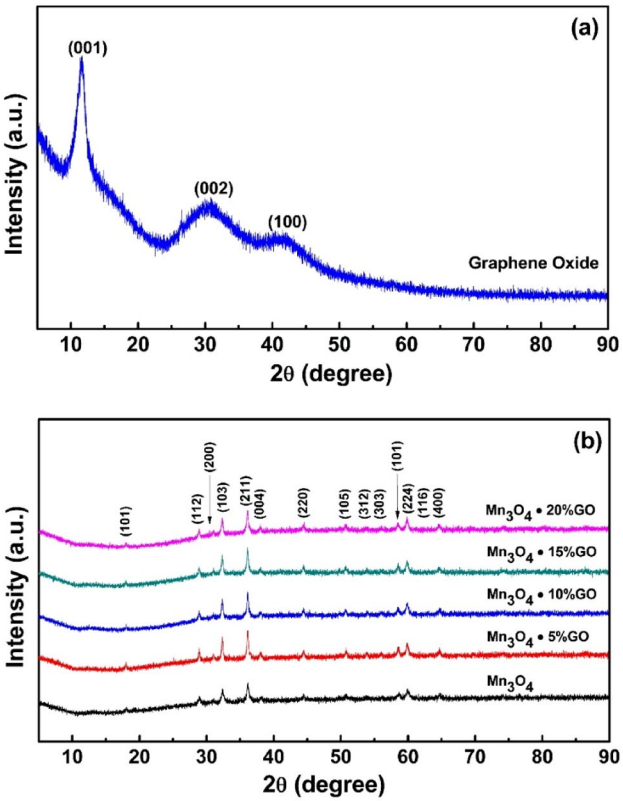

Fig. 1 X-Ray Diffraction Patterns of **a** Graphene oxide and **b** Mn_3O_4/x%GO NC's (x = 0, 5, 10, 15, 20). The diffraction peaks of Mn_3O_4/x%GO NC's are the peaks listed in the Index Card 01–080-0382

Table 3 Lattice parameters a, b and c and average crystallite size

Sample	Lattice parameter (nm)			Average crystallite size (nm)
	a	b	c	
Mn_3O_4	0.57561	0.57561	0.94323	19.87
Mn_3O_4/5%GO	0.57592	0.57592	0.94558	28.58
Mn_3O_4/10%GO	0.57603	0.57603	0.94560	26.33
Mn_3O_4/15%GO	0.57621	0.57621	0.94566	23.21
Mn_3O_4/20%GO	0.57615	0.57615	0.94610	25.21

dried at 60 °C for 12 h, resulting in the five Mn_3O_4/x% GO nanocomposites.

2.4 Characterization

Bruker D8 ADVANCE X-ray diffractometer was used to characterize the X-ray diffraction (XRD) patterns of Mn_3O_4/x% GO NC's. The 2θ was in the range of 5–90° using Cu-K_α radiation (λ = 1.5418 A°). The crystallite size was calculated by Debye–Scherrer equation for every peak to crystal planes to get more accuracy. The surface morphology of the nanoparticles and Mn_3O_4/x%GO NC's samples were determined by a scanning electron microscope of FEI model Quanta 450. The microscopic morphologies of the Mn_3O_4/x% GO NC's were observed with a JEM-3100 at the voltage of 200 kV. The preparation of the samples for TEM will start by dispersing the powders in the ethanol and then dropping the solution on carbon-coated copper grids. The Perkin Elmer Lambda-650 spectrophotometer in the range of 200–850 nm was determined the UV-visible absorption spectra in colloidal dispersion. The results of UV-visible spectra were used to calculate the energy band gap (E_g). Bruker Tensor 27 Fourier transformed infrared (FT-IR) spectrometer was used to analyst the functional group of the Mn_3O_4/x% GO samples by using the wavelength from 4000 to 400 cm^{-1}. The photoluminescence measurements (iHR 352 550 spectrometer) were operated at room temperature with a 325-nm line from a He-Cd laser as 353 the excitation source.

2.5 Photo-catalytic activity

The visible-light photo-catalytic of the five Mn_3O_4/x%GO NC's was tested by looking at the degradation of methylene blue (MB) (seen as a reduction in the intensity of the blue light). Before doing this, a calibration curve was constructed. This was done by dissolving the different amounts of MB into 80 ml of deionized water. The intensities of the blue light emitted by the MB dye were than recorded by the UV-visible spectrometer. A plot of different intensities versus the amount of the MB dye which had been dissolved in the solutions is constructed. The

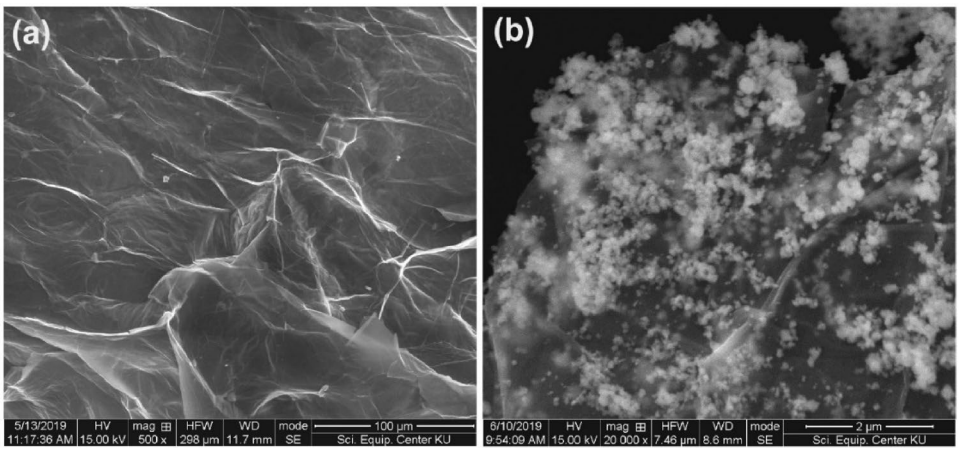

Fig. 2 SEM images of GO and Mn_3O_4/10%GO NC's: **a** SEM image of GO shows the surface of graphene oxide and **b** SEM image of a Mn_3O_4/10%GO NC's

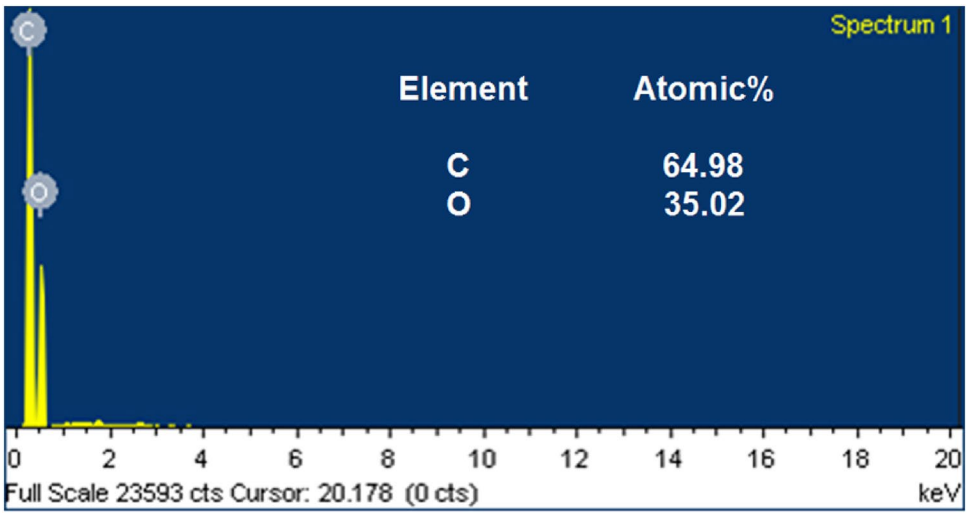

Fig. 3 Energy dispersive X-ray (EDX) spectrum of GO with the atomic percentage of C and O elements

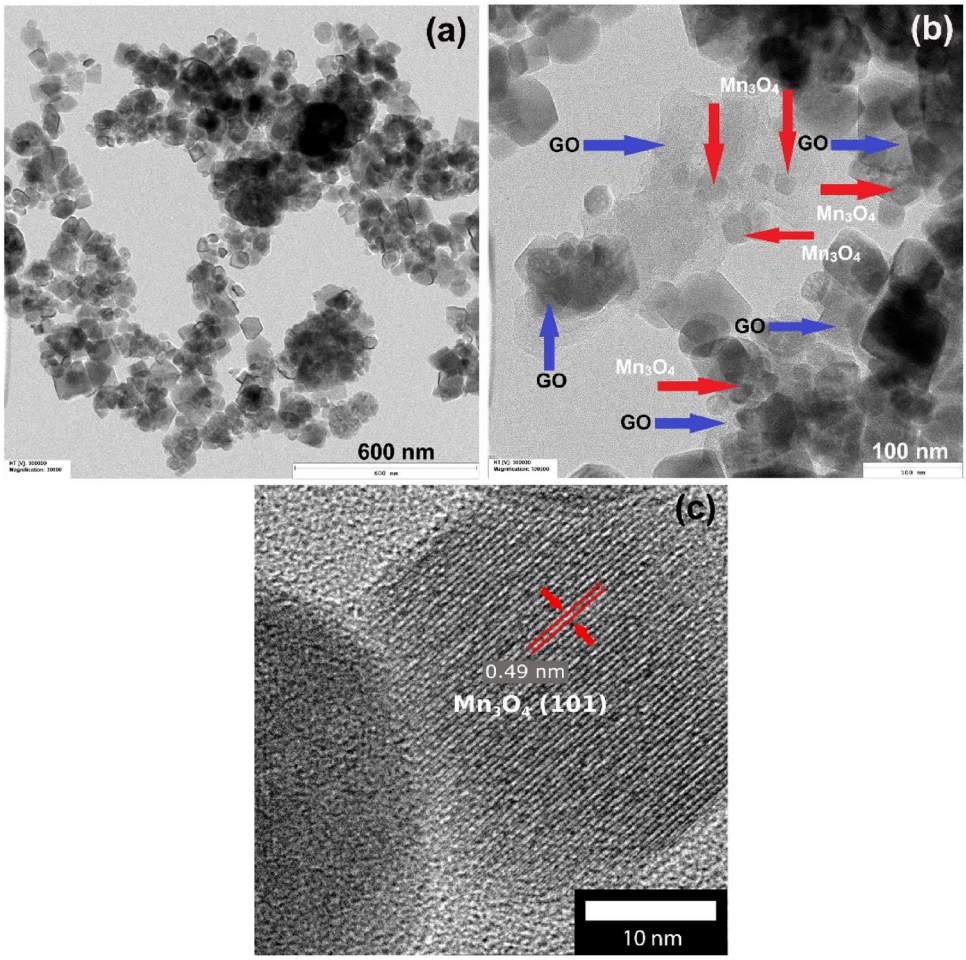

Fig. 4 TEM and HRTEM images of Mn_3O_4 NP's and Mn_3O_4/10%GO NC's**: a** TEM image of Mn_3O_4 NP's; **b** TEM image of a Mn_3O_4/10%GO NC's and **c** HRTEM of Mn_3O_4/10%GO NC's with d-spacing of Mn_3O_4 (101) plane

intensities of the blue light were used to determine the amounts of dye which were present in the solutions. To determine the photo-catalytic reduction of MB, 0.04 g of Mn_3O_4/x% GO NC's (x = 0, 5, 10, 15 and 20% by weight of GO) was dissolved in 100 ml of MB solution having MB concentration of 25 mg/l. All mixtures were stirred in the dark room for 30 min to insure the equilibrium of adsorption–desorption. Then, every mixture was emitted the light from UVA (Black light) 36 W Model: Toshiba FL40T8BL/18 W, 2 Tubes lamp. At the regular intervals, 5 ml of each mixture which had been exposed to the UVA light was removed and their UV-Vis absorptions were recorded to determine the amounts of MB which were still in the solution. The intensities of the absorption peaks centered at 614 nm and 660 nm were taken to reflect the concentration of MB remaining in solution. This information was plotted together so that by comparing the intensities of UV at the wave lengths, the amount of MB in the solutions containing the Mn_3O_4/x%GO NC's at the time of measurement could be inferred from the measured absorption. The percentage of degradation by the Mn_3O_4/x% GO NC's is calculated from Eq. (1)

$$\%\, D = \{[A(0) - A(t)] \,/\, A(0)\} x100 \quad (1)$$

where *A(t)* is the absorbance of the Visible light at 614 or 660 nm after degradation. *A(0)* is the absorbance before degradation.

Using the calibration curves which was constructed at the beginning, we have the percentage of the MB which had been photo-catalyst by the Mn_3O_4/x% GO NC's.

3 Results and discussion

3.1 Structural studies

The XRD patterns of GO and Mn_3O_4/x% GO NC's for every samples are shown in Fig. 1. Figure 1a shows the spectra of GO peaks. A strong peak at 11.56° corresponds to the reflection of the (001) plane of graphene oxide. Another small broad peak at 41.84° corresponds to the reflections of (100) plane that also belongs to graphene oxide [68, 69]. In addition, the diffraction peak (002) of GO at 30.49° was occurred when the diffraction peak (002) of graphite

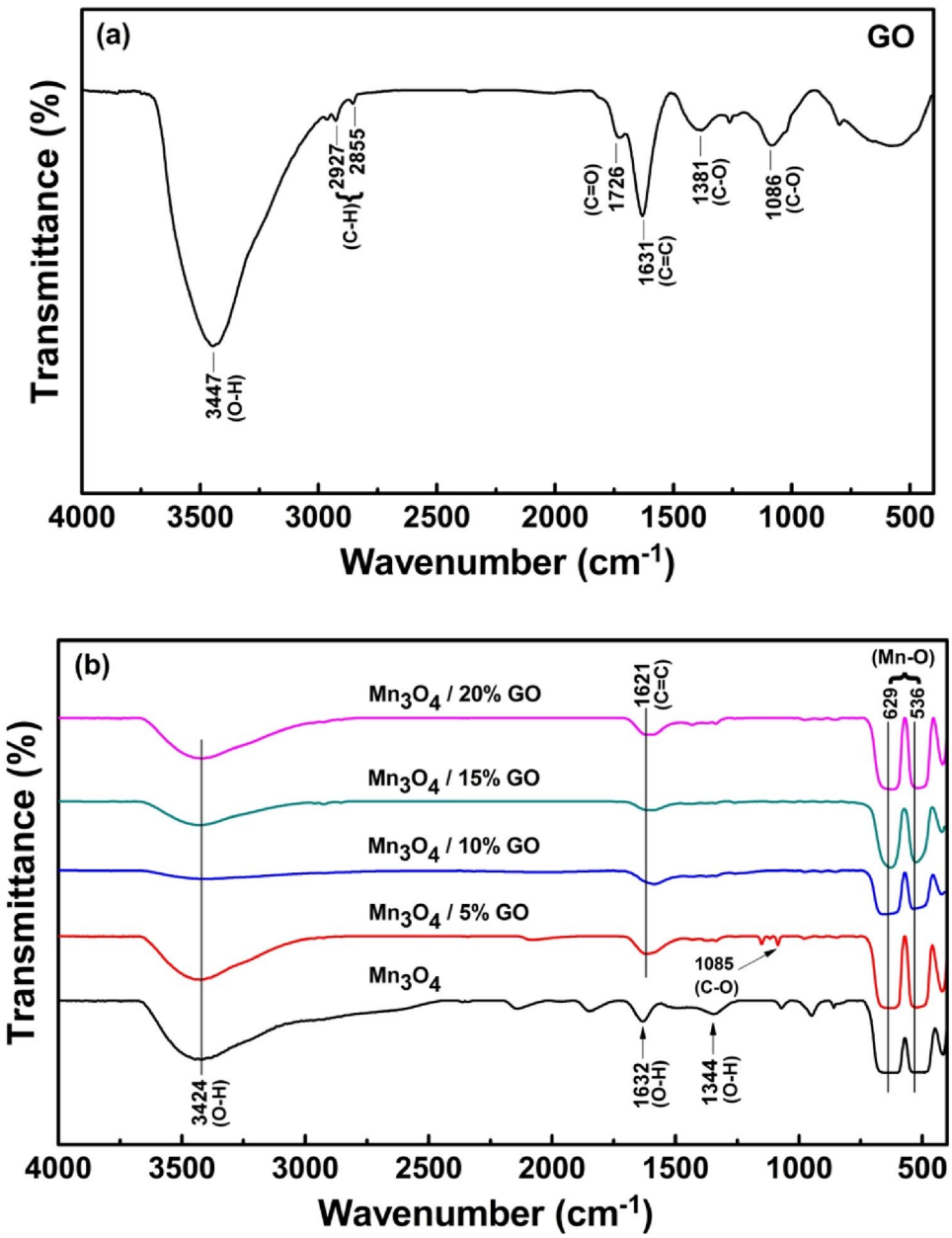

Fig. 5 Fourier Transform Infrared Absorption Data: **a** FTIR spectra for GO and **b** FTIR spectrums for the Mn_3O_4/x%GO NC's (x = 0, 5, 10, 15, 20)

crystal disappeared, indicating that the graphite had been completely oxidized to be graphene oxide. Normally, the natural graphite peak is around 26.34°. Our XRD result is similar to Liu [70]. Figure 1b obtains the XRD patterns of Mn_3O_4/x% GO NC's (x = 0, 5, 10, 15 and 20). All the peaks correspond to reflections from the (101), (112), (200), (103), (211), (004), (220), (105), (312), (303), (101), (224), (116) and (400) planes of Mn_3O_4 having a tetragonal structure which were index to the reflection planes listed on JCPDF # 01-080-0382. No any impurity phases are observed during the hydrothermal method which is suitable for the preparation of pure Mn_3O_4 phase. Moreover, there are no GO crystal phases in the Mn_3O_4/x% GO NC's. This might be due to the fact that GO are amorphous and the surfaces of GO are fully covered by Mn_3O_4 nanoparticles, resulting in the low degree of graphitization [71]. The increasing in the intensity of sharp peaks of Mn_3O_4 verifies that the prepared Mn_3O_4 particles are well crystallized and the increasing of Mn_3O_4 ratio relative to GO indicated more disordered graphene sheets. The lattice parameters **a**, **b** and **c** can be easily determined by each peak from XRD patterns. This was done for the different NC's that are revealed in Table 3. The data of lattice parameters **a**, **b** and **c** are similar to those given on the Index Card 01-080-0382. The lattice parameter **c** of the Mn_3O_4 decorating the GO does not change when the amount of GO in the NC's increased. No impurity peaks related to other phases were seen, indicating the high purity of the product. The

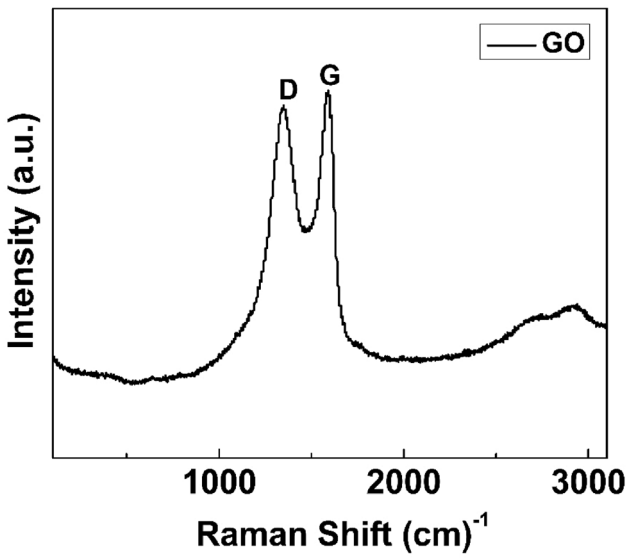

Fig. 6 Raman spectrum of graphene oxide

Scherrer formula is used to calculate the crystallite size of the peaks of the Mn_3O_4/x%GO NC's. The result is determined in Table 3. As we see, the calculation of the average crystallite size of Mn_3O_4 is 19.87 nm. When the percentage of graphene oxide increased, the average crystallite size of Mn_3O_4 NP's appears to decrease. The explanation for this is to stop the growth of Mn_3O_4 atom. Normally, the peak shift and the peak width come from the lattice distortion and the decreasing of the crystallite size.

3.2 Morphology of Mn_3O_4/x%GO NC's

The morphology of GO and Mn_3O_4/x%GO NC's was determined by Scanning Electron Microscope (SEM). Figure 2a shows the morphology of the GO. One can see that the surface of GO sheet is jagged, i.e., it is not smooth. Figure 2b shows the morphology of the Mn_3O_4/10%GO NC's. The small Mn_3O_4 NP's have grown on the surface of GO sheet. Moreover, the SEM image in Fig. 2b also shows that the Mn_3O_4 NP's are distributed over the surface of the GO with very little agglomerations of the particles on the surface of GO sheet. SEM images for the other Mn_3O_4/x%GO NC's are similar. In addition, the energy dispersive x-ray (EDX) measurement will be one method to determine the amount of C and O of GO. Figure 3 shows the spectrum of GO. As is seen, the EDX spectrum of GO investigates the presence of both C and O. The atomic percentage ratio of C and O is 64.98 and 35.02, respectively. This result is similar to Kumar [72]. TEM and HRTEM analyses provide more details about the morphology of the samples. Figure 4 shows TEM images of Mn_3O_4 NP's and Mn_3O_4/10%GO NC's. From these Figures, they investigate the information of dispersion and crystalline of NP's. Figure 4a shows the dispersion of spherical Mn_3O_4 NP's and some NP's are agglomeration. Figure 4b shows the size distribution of dispersed Mn_3O_4 NP's which is in the range of 17–24 nm. This result is similar to the average crystallite size from XRD. The lattice fringe of nanoparticle in Fig. 4c belongs to the Mn_3O_4 NP's and the interplanar d-spacing of Mn_3O_4 NP's equals to 0.49 nm which relates to the (101) plane.

3.3 Fourier transform Infrared spectrum and Raman spectroscopy

FTIR spectra provides information on the nature of the chemical bond and on the functional groups attached to the surfaces of the two components GO and Mn_3O_4, forming the composites. Figure 5a reveals the FTIR spectra for GO. The dips in the spectra between 4000 and 400 cm^{-1} provides information about the vibrations present in GO. The board peak at 3447 cm^{-1} is reported the symmetric stretching vibrational mode of the hydroxyl groups of GO. The peaks located at 2927 and 2855 cm^{-1} are corresponded to the C–H stretching modes of the cross link molecules. The C = O vibrational modes of the carbonyl groups or carboxyl groups appears at 1726 cm^{-1}. The C = C stretching shows the peak at 1631 cm^{-1}. Moreover, the two peaks at 1381 and 1086 cm^{-1} are assigned to C–O vibrational modes. Figure 5b obtains the FTIR of Mn_3O_4 NP's and Mn_3O_4·x%GO NC's. The peaks at 3424, 1632 and 1344 cm^{-1} are the stretching vibrational mode of O–H bond when water is absorbed on the surface of the Mn_3O_4 NP's. The absorption peaks observed the Mn–O stretching modes at 629 and 536 cm^{-1}. This mode is due to the tetrahedral and octahedral sites in the NC's crystal structure. The bonding between the Mn_3O_4 and the GO sheet would be occurred at Mn–O–C bond (or Mn–O–C junction). Looking at the FTIR spectra for Mn_3O_4, we do not see any dips assigned to an O–C bond. Looking at the spectra for GO, we see a dip to an O–C band at 1086 cm^{-1}. Furthermore, when we look at the spectra of 5%GO NC's, we see two dips close to 1085 cm^{-1}. The right most dip may be due to the O–C vibration in GO. The second peak may be due to O–C vibration in the Mn–O–C bond. This junction that connects the NP to the GO could also be responsible for the strain. Mn–O–C bond would pull the Mn ion in the Mn_3O_4 NP's towards the GO sheet but there is no force pulling the ion in the opposite direction. Raman spectrum of GO is presented in Fig. 6. GO has intense D and G bands. The G band is more intense than the D band. The G band represents the intensity at 1596 cm^{-1} which is the in plane bond stretching motion of pairs of C sp^2 atoms while the D band located at 1358 cm^{-1} corresponds to the defects and disorder carbon in the graphite layers [73]. The intensity ratio of the D to the G band (I_D/I_G) provides a sensitive

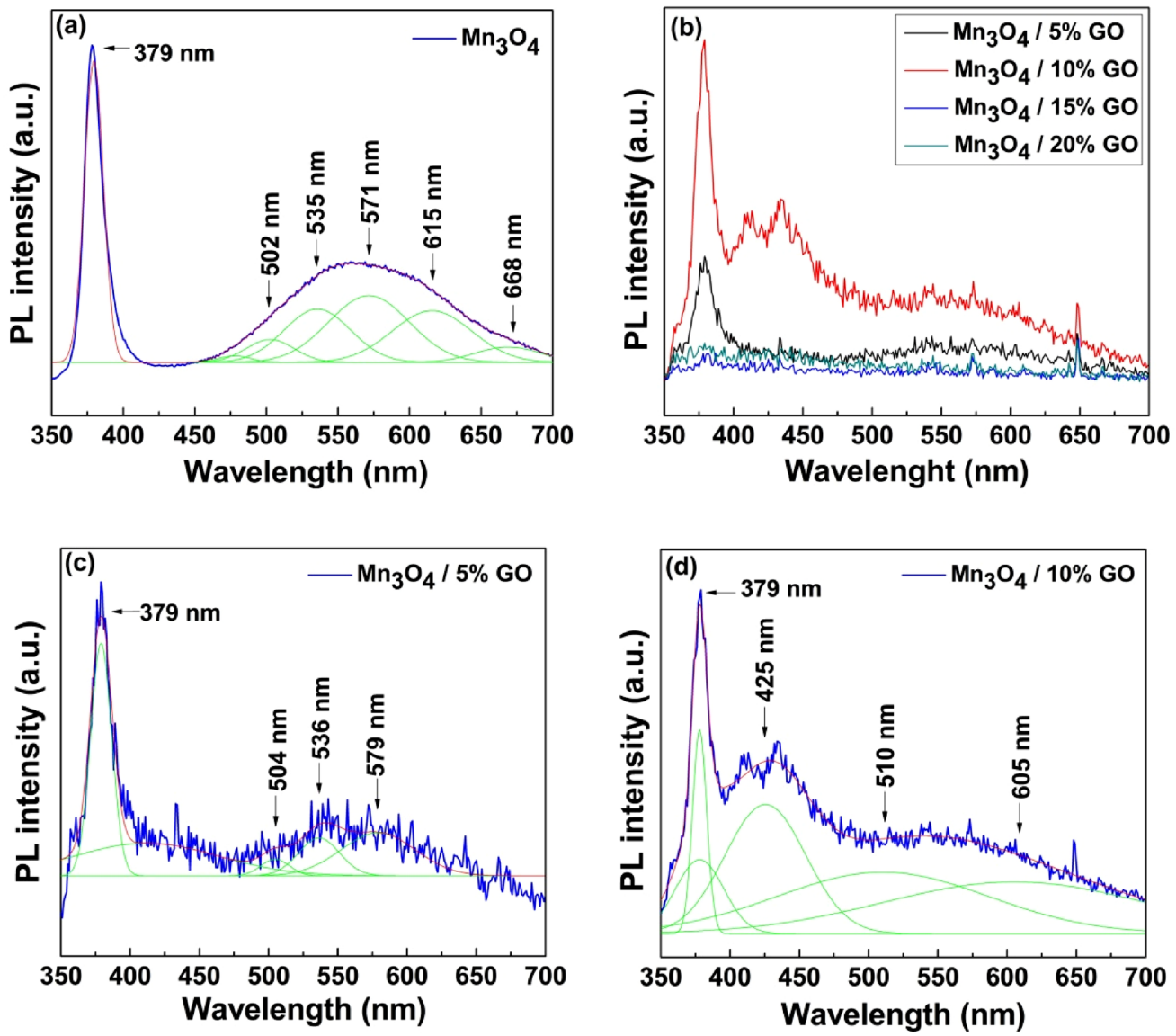

Fig. 7 Photoluminescence spectra of **a** Mn_3O_4 NP's; **b** PL spectra of the Mn_3O_4/x%GO NC's (x = 5, 10, 15, 20); **c** PL spectra for the Mn_3O_4/5%GO NC's and **d** PL spectra for the Mn_3O_4/10%GO NC's

measure of the disorder and crystallite size of the graphitic layers. The intensity ratio I_D/I_G of GO is 0.85.

3.4 Photoluminescence spectra

The photoluminescence spectra of Mn_3O_4 NP's and Mn_3O_4/x%GO NC's were measured by an excitation wavelength of 325 nm at room temperature (see Fig. 7). Figure 7a is the PL spectrum for pure Mn_3O_4 NP's. An exciton peak at 378 nm is clearly seen. The photoelectrons generated when the UV light is shined on the Mn_3O_4 goes into the creation of the exciton. The emission peak at 378 nm comes from the recombination of electron and hole. The emission of free excitons occurs when the process of an exciton–exciton collision process near the band edges in a well crystallized crystals [74, 75]. The emissions of PL spectrums in the visible light part are due to the electronic transitions between the defects states created the formation of defects in the crystal states of the NP's caused by the fabrication process or the introduction of impurities into the host ferrites. The visible light emission spectrums for each of the NC's are the superposition of the emissions from the different defects which are formed in the different NC's. The PL emission spectrums for the as-prepared Mn_3O_4 NP's could be decomposed into five Gaussian peaks at 502 nm, 515 nm, 571 nm 615 and 668 nm. The PL emission located at 571 nm belongs to the yellow emission which is due to the d–d transitions connecting to the

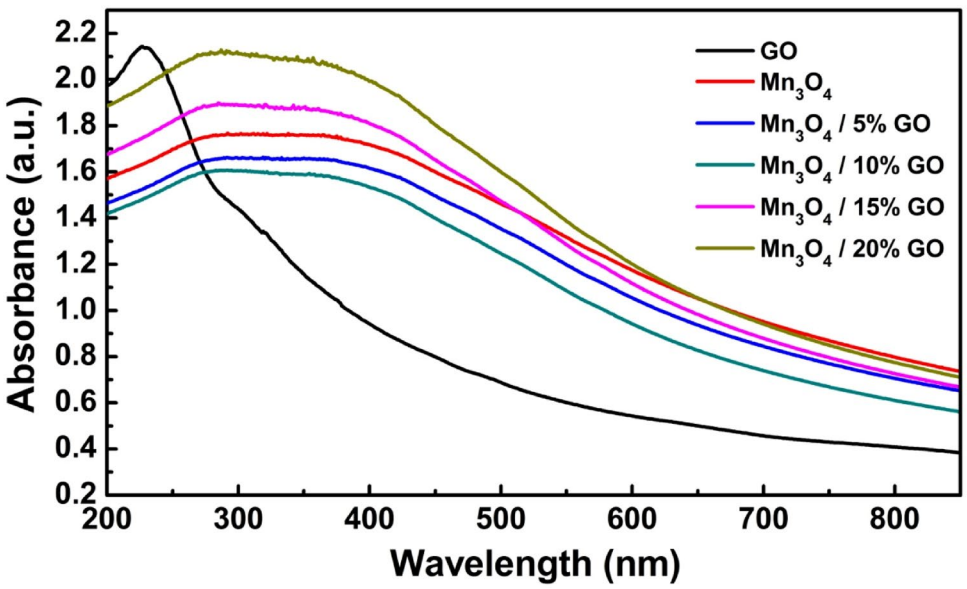

Fig. 8 UV-Vis absorption by GO and the Mn_3O_4/x%GO NC's (x = 0, 5, 10, 15, 20)

Mn^{3+} ions [47]. For the broad green emission, it appears at 535 nm and the broad red emission observed at 615 nm are due to the radial recombination of photo-generated hole with an electron. This may be help to produce the surface defect or surface dangling bonds on the surface of NP's [75]. From the structural analysis, we believe that the highly photoluminescent response comes from the abundant defects that builds by the Jahn–Teller distortion of Mn^{3+} ion in the self-assembled NP's and it also corresponds to d–d transitions. The fact of this reason is the ground state of Mn^{3+} ion is split by using the strong static Jahn–Teller effect [76]. Figure 7b shows that two separate trends are occurring when the coverage of the GO surface by the NP's. When the percentage of GO in the composite increased, the spectrum of PL emission seems to be decreased. This may be due to two reasons: (1) a decrease in the heights of the exciton peak or to (2) a decrease in the defect emission from the NP's. In Fig. 7b, the decrease in the heights of the exciton peaks in PL spectra of the 5% and 10% NC's and the complete absence in the 15% and 20% NC's means that no photoelectrons are needed for the creation of the excitons and that all the photoelectrons are available for the photo-catalytic activity. The number of photoelectrons created depends on the number of Mn_3O_4 NP's on a given area of the GO sheet. As the amount of GO increases, the density or number of NP's decreases. The decrease in parts of the spectra due to the defect (visible light spectra) of the PL spectra with the increased coverage of the GO surface would imply that there was a lessening of the interaction between the Mn_3O_4 crystal and the GO sheet (due to the fact that there is lesser NP per unit area of the GO surface). The results in Fig. 7c and d are different. This is because there are still Mn_3O_4 NP crystals on the GO surface. This is indicated by the relative heights of the different Gaussian curve as seen in the Fourier decompositions of the visible light portions of the PL spectrums for the different NC's. Looking at Fig. 7c, the Gaussian peaks correspond to the green emission (504 nm, 536 nm) and yellow emission (579 nm). The PL spectra for Gaussian peaks of the Mn_3O_4/10%GO NC's only show the violet-red emission (605 nm) as shown in Fig. 7. This emission was ones observed only in the excitation of the host ferrite. Moreover, the intensity peak in PL spectra for the peak position at 425 nm is in blue emission and this may be the possible defect of Mn vacancy which is in the Mn^{2+} tetrahedral and Mn^{3+} octahedral sites. For another peak at 510 nm, it is in the green emission which comes from the oxygen vacancy. Sarma et al. [77, 78] reported in their two studies that the red-shift of the Mn emission comes from the ligand field interactions and that the shifting of the Mn d–d emission may be came from the hosts which have multiple ions in the crystal lattices that would distort the Mn coordinates and have an effect on the emission energy.

3.5 UV-Vis absorption by the Mn_3O_4/GO NC's

The photo-catalytic performance of the Mn_3O_4/x%GO (x = 0, 5, 10, 15, 20) NC's was studied. The dependencies of the catalytic efficiency on the different reaction parameters were investigated. The photo-catalytic activity of the Mn_3O_4/x%GO (x = 0, 5, 10, 15, 20) NC's was determined by the photo degradation of the dye methylene blue (MB). All the degradations were conducted under UV–irradiation. The photo-catalytic reaction can be deduced from the transmission of UV-visible light through a solution containing only GO sheet and the solutions containing

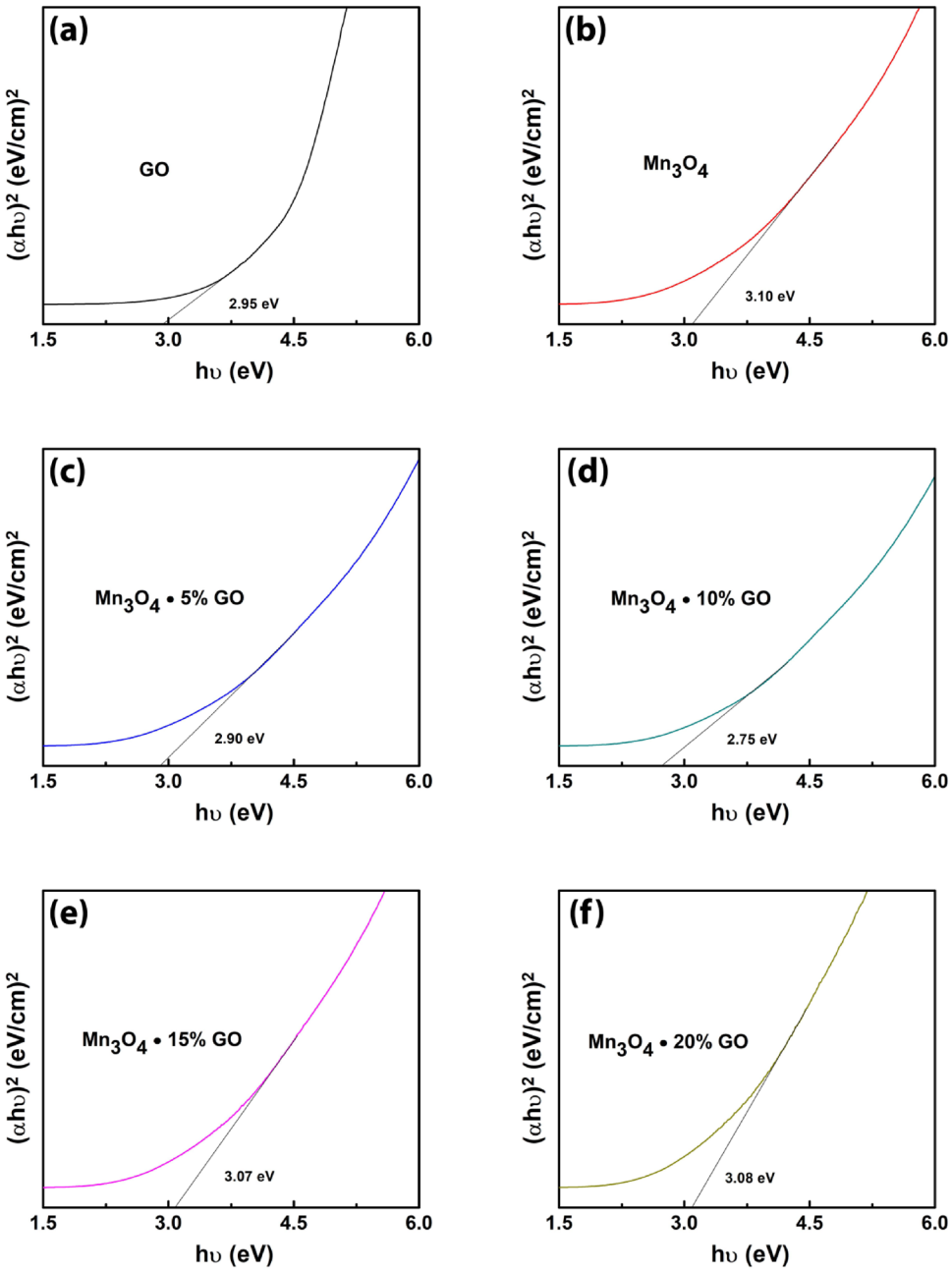

Fig. 9 Tauc's plots of the absorption data for Go and the Mn_3O_4/x%GO NC's

Table 4 Energy gaps of Mn_3O_4/x%GO NC's (x = 0, 5, 10, 15, 20) by extrapolating the linear portion of Tauc plots of the UV-visible absorptions of each NC's

Sample	Energy band gap (eV)
GO	2.95
Mn_3O_4	3.10
Mn_3O_4/5%GO	2.90
Mn_3O_4/10%GO	2.75
Mn_3O_4/15%GO	3.07
Mn_3O_4/20%GO	3.08

the Mn_3O_4/x%GO NC's. The absorption spectra are seen in Fig. 8. The UV-visible absorption spectra of NC samples suggest the strong absorption in the visible light region. The spectra of Mn_3O_4/x%GO NC's exhibit broad bands from 250 to 550 nm. These occur from d-d crystal field transitions of the tetrahedral Mn^{3+} species and from the distortion in the lattice crystal structure. From UV-Vis data, band gap energy of the samples is determined from the plot of the Eq. (2) as follow:

$$\alpha h\nu = A\left(h\nu - E_g\right)^n \quad (2)$$

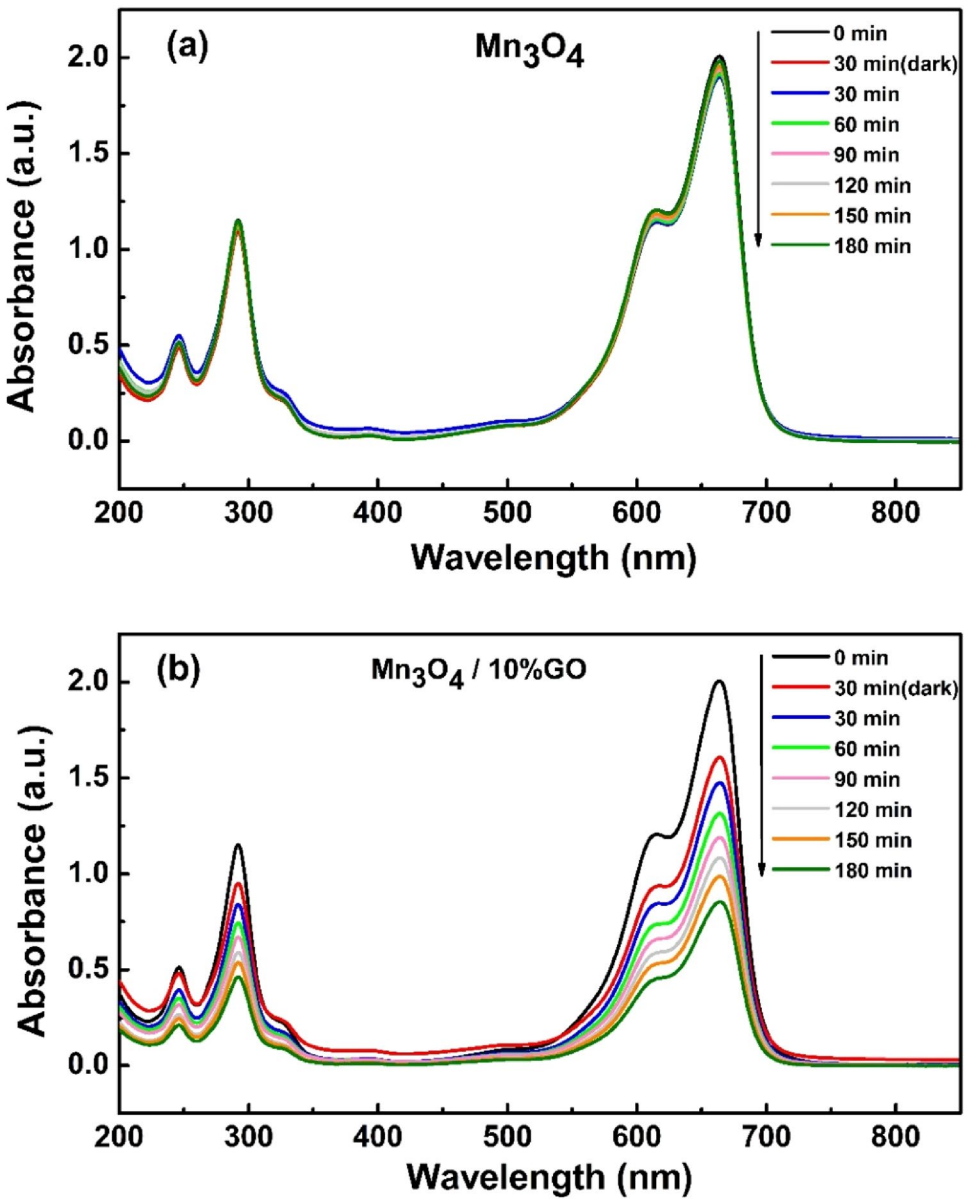

Fig. 10 Absorption spectra of the MB solutions containing: **a** Mn_3O_4 NP's and **b** Mn_3O_4/10%GO NC's after they were exposed to the laser radiation for different amounts of time

where v is respectively light frequency, α is absorption coefficient, E_g is band-gap energy, and A is a constant, n is ½ for direct allowed transitions and 2 indirect allowed transitions.

Tauc curves which are the plots of Eq. (2) are shown in Fig. 9. We calculated by using direct band gap ($n = ½$). Extrapolating the linear portions of the linear part of these Tauc curves which is the energy gap can be obtained. From these results, we can see that the energy band gaps of Mn_3O_4/x%GO NC's changed. The values of the energy band gaps reveal in Table 4. As we seen, the changing in the energy gap is due to the change in the strain within the nano clusters when the Mn_3O_4 NP's are linked to the GO sheets. The information on the absorbance can also be used to determine the photocatalytic reduction of methylene blue (MB). The degradation of MB can be determined by recording the initial intensities of the blue light at emitted by solutions containing a fixed amount of the MB before exposing the solution to incident beam of light when the absorbance occurs. The absorbance for Mn_3O_4 NP's and Mn_3O_4/10%GO NC's are shown in Fig. 10. In Fig. 10a, no degradation by the solutions having only Mn_3O_4 NP's was seen. This may be due to the fact that the photoelectrons created by the illumination of the NP's did not transfer to the GO since there was no GO present. Moreover, the surface of the NP's is small, the probability of a photochemical reaction between the photoelectrons on the NP's and MB molecules would very small.When the Mn_3O_4 NP's decorate the surface of the GO sheets, photoelectrons on the NP's can migrate to the surface of the GO

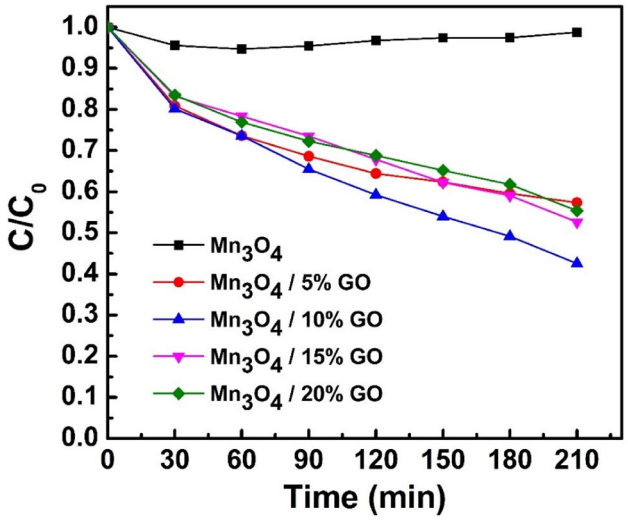

Fig. 11 Normalized concentration of MB solution for photocatalytic degradation by the Mn_3O_4 and Mn_3O_4/x%GO NC's (x = 0, 5, 10, 15, 20)

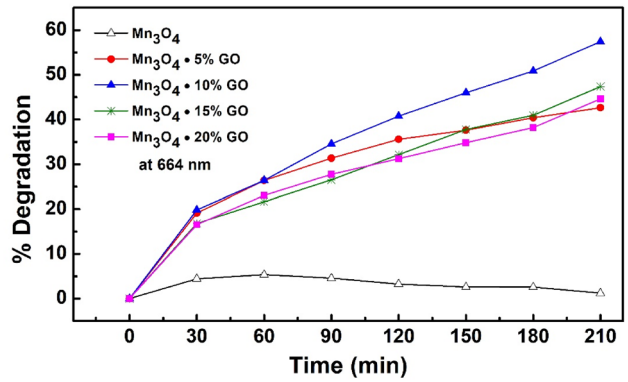

Fig. 12 The % degradation of methylene blue versus time for Mn_3O_4 NP's and Mn_3O_4/x%GO NC's

so that there are now photoelectrons on the GO surface. These photoelectrons on the surface can now catalysis the MB molecules since the larger surface area of the GO increases the possibility of the MB molecule coming in contact with the photoelectrons which are now on the GO. We would observe a reducing in the intensity of the blue color (See the degradation of MB the Mn_3O_4/10% GO mixture demonstrated in Fig. 10b. Plotting the degradation of the different NC's at the different times, we get the activities of the NC's for the reduction of MB as shown in Fig. 11. From the curves, we see that the best degradation was achieved with the Mn_3O_4/10%GO NC's. It is interesting to note that Mn_3O_4 prepared by hydrothermal method had no catalytic activity. This may be due to the large size of the particle, no dispersion in water and incompatible with energy band gap. Moreover, the development of the photo-catalytic activity of the Mn_3O_4 NP's can be done by using them decorate onto the GO sheets. Then, the photo-catalytic reaction will appear on the surface of GO sheet instead of the surfaces of the NP's. Zhang et al. [79], suggested that the enhancement of photo-catalytic reaction is due to the increased absorptivity of the dye to the surface of the GO sheets. The improvement of absorptivity may come from the strong π-π conjugation of the dye molecules and the aromatic regions of graphene. The photocatalytic degradation of Mn_3O_4 and Mn_3O_4/x%GO NC's was studied by using the methylene blue (MB) dye at room temperature as shown in Fig. 12. The result shows that the percent (%) of degradation of methylene blue for Mn_3O_4 was low. This may be due to aggregate of Mn_3O_4 NP's, resulting in low reaction on the surface area. For Mn_3O_4/x%GO NC's, the percent (%) of degradation of methylene blue is much higher than Mn_3O_4. This is because the GO sheet is large in surface area and the Mn_3O_4 NP's can be easily distributed on the surface of GO, resulting in high reaction on surface of GO. Moreover, we can see that Mn_3O_4/10%GO NC's has an excellent the percent (%) of degradation of methylene blue compared to the other samples. The schematic of the Mn_3O_4/x%GO NC's is shown in Fig. 13. In general, the amounts of Mn_3O_4 NP's will aggregate on GO sheets which lead to decreased photocatalytic activity. The mechanism process of photocatalytic activity of Mn_3O_4 NP's and Mn_3O_4/x%GO NC's as shown in Eqs. (3) to (9).

$$Mn_3O_4 + h\nu \rightarrow Mn_3O_4(e^-) + Mn_3O_4\left(h^+\right) \quad (3)$$

$$Mn_3O_4(e^-) + GO \rightarrow GO(e^-) \quad (4)$$

$$Mn_3O_4\left(h^+\right) + H_2O \rightarrow {}^{\bullet}OH + H^+ \quad (5)$$

$$GO(e^-) + O_2 \rightarrow O_2^{\bullet -} \quad (6)$$

$${}^{\bullet}OH + {}^{\bullet}OH \rightarrow H_2O_2 \quad (7)$$

$$H_2O_2 + O_2^{\bullet -} \rightarrow {}^{\bullet}OH + {}^{-}OH + O_2 \quad (8)$$

$$MB + {}^{\bullet}OH \rightarrow CO_2 + H_2O \quad (9)$$

The Mn_3O_4 NP's resting on top of GO sheet with an occupied valence band (VB) state and an unoccupied conduction band (CB) state. When Mn_3O_4 NP's are stimulated by photon energy; the electron in VB state will excite to CB state. This can be made hole in VB and the electrons in CB state will be transferred into the GO sheet. Therefore, GO sheet will serve as good accepter and electron

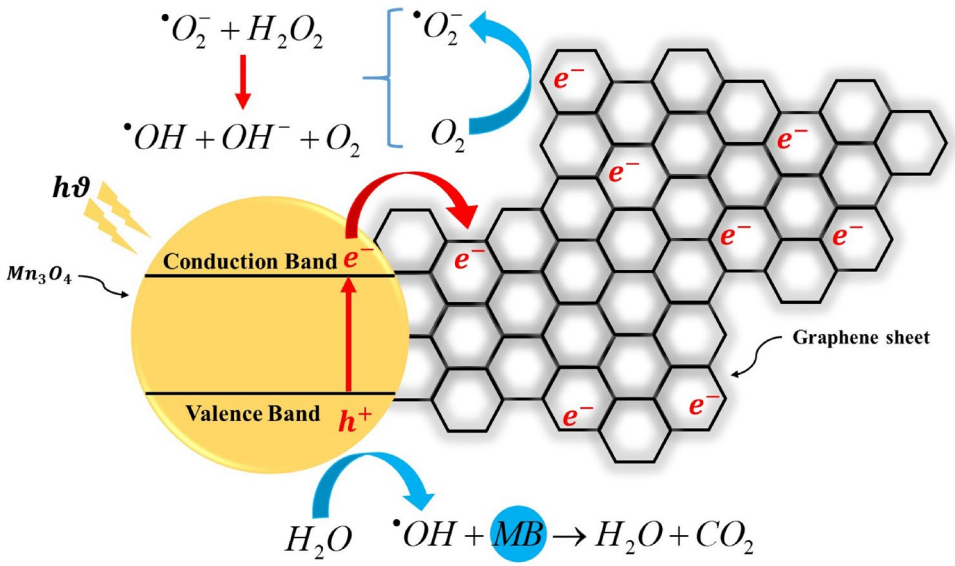

Fig. 13 Schematic of a Mn_3O_4/x%GO NC's

transferred which can help electrons move freely on the GO sheet. This result will interrupt the recombination of electrons and holes. The holes which occupied in the VB state will form the oxidation process by oxidizing H_2O or OH^- to be $^{\bullet}OH$ and then $^{\bullet}OH$ can form a combination of H_2O_2. On the other hand, the electrons are on the GO sheet will make the reduction reaction by binding with O_2 in the water to create the $^{\bullet}O_2^-$ and to react with H_2O_2 to be $^{\bullet}OH$. This $^{\bullet}OH$ is the degradation molecule of methylene blue which reacts with methylene to be CO_2 and H_2O. Prior to the formation pair and after its annihilation, the photo-electron e^- can move to the surface of the NP where it can interact with any chemical ions which are present in the solvent. Of course, the chemical reactions can only occur if the photoelectron and chemical specie meet at the same time and the same place. Since, the sizes of the NP's and chemical ions are both small and are randomly moving in the liquid, the joint encounter of the two will be small and the photo-catalytic reaction would be slow. When the NP's are attached to GO, the photo excited electron can cross the bridge (junction) connecting the NP and the GO. In the TiO_2 decorated rGO, the bridge is the Ti–O–C bond [17] while in the ZnO decorated rGO, it is the Zn–O–C bond [18]. In this present case, the junction is a Mn–O–C chemical bond. The photoelectrons can travel freely in the 2D carbon array in the GO (keeping in mind that the 2D hexagonal carbon array is a very good conductor). If the moving photoelectron encounters the same chemical ion just mentioned, the two would undergo the same chemical action as before. Because the area of the GO is much more than the area of the nanoparticle surface, the probability of the photoelectron and the chemical specie encountering would be greater on the GO surface than that on the surface of the NP. This would lead the photo-catalytic activity being enhanced. Because of the difference in the mobility's of the electrons and holes, charge separation will occur and when this happens, one encounters a suppression of the annihilation of electron/hole pairs and therefore an increase in the photo-catalytic activity. This was the explanations given by Patra et al. [80], for the enhanced solar generation by MoS_2/GO and MoS_2/MoS_{3-x}/GO multi-functional NC's, for solar water splitting by Au-Pd/rGO/TiO_2 hetero junctions by Tudu et al. [81], and by Au-RGO/N-RGO-TiO_2 hetero junctions by Bharad et al. [82].

4 Conclusion

In conclusion, the Mn_3O_4/x%GO NC's has been successfully fabricated by the hydrothermal method. SEM image showed that the Mn_3O_4 NP's were distributed over the surface of the GO sheet and the EDX confirmed the result of GO sheet. HRTEM investigation showed that the GO layers were interfacing with the Mn_3O_4 NP's where a chemical interaction between the two could be created. FT-IR results investigated the bonding between Mn_3O_4 and GO sheet and this bonding may be due to O-C vibration in the Mn–O–C bond which connects the Mn_3O_4 NP's to the GO sheet together. PL emission which is in the violet–red luminescent region shows the creation of defects in the fabricated Mn_3O_4 NP's nanostructures. These defects create the defect states to which electrons in the VB can be excited to when the CB. For the blue emission, it may be the possible defect of Mn vacancy which is in the Mn^{2+} tetrahedral and Mn^{3+} octahedral sites and the peak is in the green emission which comes from the oxygen vacancy. The best degradation efficiency was achieved by the Mn_3O

NP's when they were used to decorate the GO sheets in the Mn_3O_4/10%GO NC's solution. Both the $FTIR_4$ results and HRTEM images provided evidence that this NC had the best number of Mn–O–C bonds between the GO sheets and Mn_3O_4 NP's. These bonds would facilitate the transfer of the photoelectrons from the surfaces of the NP's to the GO sheets.

Acknowledgements We would like to thank Faculty of Science, Kasetsart University and Department of Physics for the financial support. Finally, we also thank to King Mongkut's University of Technology Thonburi for the financial support provided by through the KMUTT 55th Anniversary Commemorative Fund.

Data and materials availability All data needed to evaluate the conclusions in the paper are present in the paper. Additional data related to this paper may be requested from the authors.

Declaration

Conflicts of interest The authors declare that there are no conflicts of interest regarding the publication of this paper.

References

1. Du X, Skachko I, Barker A, Andrei EY (2008) Approaching ballistic transport in suspended graphene. Nat Nanotechnol 3:491–495. https://doi.org/10.1038/nnano.2008.199
2. Lee C, Wei X, Kysar JW, Hone J (2008) Measurement of the elastic properties and intrinsic strength of monolayer graphene. Science 321:385. https://doi.org/10.1126/science.1157996
3. Balandin AA, Ghosh S, Bao W, Calizo I, Teweldebrhan D, Miao F, Lau CN (2008) Superior thermal conductivity of single-layer graphene. Nano Lett 8(3):902–907. https://doi.org/10.1021/nl073187 2
4. Kumar R, Oh JH, Kim HJ, Jung JH, Jung CH, Hong WG, Kim HJ, Park JYOH, IK (2015) Nanohole-structured and palladium-embedded 3D porous graphene for ultrahigh hydrogen storage and CO oxidation multi-functionalities. ACS Nano 9(7):7343–7351. https://doi.org/10.1021/acsnano.5b02337
5. Kumar RJ, Abdel-Galeil MM, Ya KZ, Fujita K, Tan WK, Matsuda A (2019) Facile and fast microwave-assisted formation of reduced graphene oxide-wrapped manganese cobaltite ternary hybrids as improved supercapacitor electrode material. Appl Surf Sci 481:296–306. https://doi.org/10.1016/j.apsusc.2019.03.085
6. Kumar RJ, Youssry SM, Yaa KZ, Tanc WK, Kawamura G, Matsuda A (2020) Microwave-assisted synthesis of Mn_3O_4–Fe_2O_3/Fe_3O_4@rGO ternary hybrids and electrochemical performance for supercapacitor electrode. Diam Relat Mater 101:107622. https://doi.org/10.1016/j.diamond.2019.107622
7. Kumar RJ, Matsuo R, Kishida K, Abdel-Galeil MM, Suda Y, Matsuda A (2019) Homogeneous reduced graphene oxide supported NiO-MnO_2 ternary hybrids for electrode materials with improved capacitive performance. Electrochim Acta 303:246–256. https://doi.org/10.1016/j.electacta.2019.02.084
8. El-Hallag IS, El-Nahass MN, Youssry SM, Kumar RJ, Abdel- Galeil MM, Matsuda A (2019) Facile in-situ simultaneous electrochemical reduction and deposition of reduced graphene oxide embedded palladium nanoparticles as high performance electrode materials for supercapacitor with excellent rate capability. Electrochim Acta 314:124–134. https://doi.org/10.1016/j.electacta.2019.05.065
9. Kumar R, Sahoo S, Joanni E, Singh RK, Maegawa K, Tan WK, Kawamura Go, Kar KK, Matsuda A (2020) Graphene engineering for energy storage and conversion. Mater Today 39:47–65. https://doi.org/10.1016/j.mattod.2020.04.010
10. Kumar RJ, Sumanta Sahoo S, Joanni E, Singh RK, Yadav RM, Verma RK, Singh DP, Tan WK, Pérez del Pino A, Moshkalev SA, Matsuda A (2019) A review on synthesis of graphene, h-BN and MoS_2 for energy storage applications: recent progress and perspectives. Nano Res 12(11):2655–2694. https://doi.org/10.1007/s12274-019-2467-8
11. Kumar RJ, Sahoo S, Joanni E, Singh RK, Tan WK, Kar KK, Matsuda A (2019) Recent progress in the synthesis of graphene and derived materials for next generation electrodes of high performance lithium ion batteries. Prog Energy Combust Sci 75:100786. https://doi.org/10.1016/j.pecs.2019.10078
12. Gupta PK, Chauhan D, Khan ZH, Solanki PR (2020) ZrO_2 Nanoflowers decorated with graphene quantum dots for electrochemical immunosensing. ACS Appl Nano Mater 3:2506–2516. https://doi.org/10.1021/acsanm.9b02598
13. Huang WH, Li XM, Yang XF, Zhang HY, Liu PB, Ma YM, Lu X (2020) CeO_2-embedded mesoporous CoS/MoS_2 as highly efficient and robust oxygen evolution electrocatalyst. Chem Eng J. https://doi.org/10.1016/j.cej.2020.127595
14. Zhou WJ, Wu XJ, Cao XH, Huang X, Tan CL, Tian J, Liu H, Wang JY, Zhang H (2013) Ni_3S_2 nanorods/Ni foam composite electrode with low over potential for electrocatalytic oxygen evolution. Energy Environ Sci 6:2921–2924. https://doi.org/10.1039/C3EE41572D
15. Huang WH, Li XM, Yu DY, Yang XF, Wang LF, Liu PB, Zhang J (2020) CoMo-bimetallic N-doped porous carbon materials embedded with highly dispersed Pt nanoparticles as pH-universal hydrogen evolution reaction electrocatalyst. Nanoscale 12:19804–19813. https://doi.org/10.1039/D0NR04418K
16. Li JG, Xie KF, Sun HC, Li ZS, Ao X, Chen ZH, Ostrikov KK, Wang CD, Zhang WD (2019) Template-directed bifunctional dodecahedral CoP/CN@MoS_2 electrocatalyst for high efficient water splitting. ACS Appl Mater Interfaces 11:36649–36657. https://doi.org/10.1021/acsami.9b11859
17. Khamboonrueang D, Srirattanapibul S, Tang IM, Thongmee S (2018) TiO_2·rGO nanocomposite as a photo catalyst for the reduction of Cr^{6+} Mater. Res Bull 107:236–241. https://doi.org/10.1016/j.materresbull.2018.07.002
18. Srirattanapibul S, Tang IM, Thongmee S (2020) Photo catalytic reduction of Cr^{6+} by ZnO decorated on reduced graphene oxide (rGO) Nanocomposites. Mater Res Bull 122:110705. https://doi.org/10.1016/j.materresbull.2019.110705
19. Singh N, Prakash J, Gupta RK (2017) Design and engineering of high-performance phtocatalytic systems based on metal oxide-grahene-noble metal nanocomposites. Mol Sys Des Eng 2:422–439. https://doi.org/10.1039/C7ME00038C

20. Adineh E, Rasuli R (2015) Facile synthesis of decorated graphene oxide sheets with WO_3 nanoparticles. Appl Phys A 120:1587–1592. https://doi.org/10.1007/s00339-015-9359-x
21. Torkaman M, Rasuli R, Taran L (2020) Photovoltaic and photocatalytic performance of anchored oxygen-deficient TiO_2 nanoparticles on graphene oxide. Results Phys 18:103229. https://doi.org/10.1016/j.rinp.2020.103229
22. Kumar RJ, Singh RK, Dubey PK, Kumar P, Tiwari RS, Oh IK (2013) Pressure-dependent synthesis of high-quality few-layergraphene by plasma-enhanced arc discharge and their thermal stability. J Nanopart Res 15:1847. https://doi.org/10.1007/s11051-013-1847-3
23. Kumar RJ, Singh RK, Singh DP, Joanni E, Yadav RM, Moshkalev SA (2017) Laser-assisted synthesis, reduction and micro-patterning of graphene: Recent progress and applications. Coord Chem Rev 342:34–79. https://doi.org/10.1016/j.ccr.2017.03.021
24. Kumar RJ, Singh RK, Singh AK, Vaz AR, Rout CS, Moshkalev SA (2017) Facile and single step synthesis of three dimensional reduced graphene oxide-$NiCoO_2$ composite using microwave for enhanced electron field emission properties. Appl Surf Sci 416:259–265. https://doi.org/10.1016/j.apsusc.2017.04.189
25. Kumar RJ, Alaferdovb AV, Singhc RK, Singhd AK, Shahe J, Kotnalae RK, Singhd K, Sudaa Y, Moshkalev SA (2019) Self-assembled nanostructures of 3D hierarchical faceted-iron oxide containing vertical carbon nanotubes on reduced graphene oxide hybrids for enhanced electromagnetic interface shielding. Compos Part B 168:66–76. https://doi.org/10.1016/j.compositesb.2018.12.047
26. Liu PB, Gao S, Yi W, Zhou FT, Huang Y, Luo JH (2020) Metal-organic polymer coordination materials derived Co/N-doped porous carbon composites for frequency-selective microwave absorption. Compos B 202:108406. https://doi.org/10.1016/j.compositesb.2020.108406
27. Gao S, Wang Y, Huang Y, Zhou FT, Liu PZ (2021) Magnetic porous N-doped carbon composites with adjusted composition and porous microstructure for lightweight microwave absorbers. Carbon 173:655–666. https://doi.org/10.1016/j.carbon.2020.11.043
28. Awasthi K, Kumar RJ, Tiwari RS, Srivastava ON (2010) Large scale synthesis of bundles of aligned carbon nanotubes using a natural precursor: turpentineoil. J Exp Nanosci 5(6):498–508. https://doi.org/10.1080/17458081003664159
29. Kumar RJ, Abdel-Galeil MM, Ya KZ, Fujita K, Tan WK, Matsuda A (2019) Facile and fast microwave-assisted formation of reduced graphene oxide-wrapped manganese cobaltite ternary hybrids as improved supercapacitor electrode material. Appl Surf Sci 481:296–306. https://doi.org/10.1016/j.apsusc.2019.03.085
30. Choucair M, Thordarson P, Stride JA (2009) Gram-scale production of graphene based on solvothermal synthesis and sonication. Nat Nanotechn 4:30–33. https://doi.org/10.1038/nnano.2008.365
31. Singh AK, Chaudhary V, Singh AK, Sinha SRP (2020) Tailoring of electrical properties of TiO_2 decorated CVD grown single-layer graphene by HNO_3 molecular doping. Synth Met 264:116389. https://doi.org/10.1016/j.synthmet.2020.116389
32. Li XS, Cai WW, An JB, Kim S, Nah J, Yang DX, Piner R, Velamakanni A, Jung I, Tutuc E, Banerjee SK, Colombo L, Ruoff RS (2009) Large-area synthesis of high-quality and uniform graphene films on copper foils. Sci 324(5932):1312–1314. https://doi.org/10.1126/science.1171245
33. Zhang H, Lv X, Li YM, Wang Y, Li JH (2010) P25-Graphene composite as a high performance photocatalyst. ACS Nano 4:380–386. https://doi.org/10.1021/nn901221k
34. An X, Yu JC (2011) Graphene-based photocatalytic composites. RSC Adv 1:1426–1434. https://doi.org/10.1039/C5NH00113G
35. Du J, Lai X, Yang N, Zhai J, Kisailus D, Su F, Wang D, Jiang L (2011) Hierarchically ordered macro–mesoporous TiO_2–Graphene composite films: Improved tass transfer, reduced charge recombination and their enhanced photocatalytic activities. ACS Nano 5:590–596. https://doi.org/10.1021/nn102767d
36. Wang D, Choi D, Li J, Yang Z, Nie Z, Kou R, Hu D, Wang C, Saraf LV, Zhang J et al (2009) Self-assembled TiO_2–Graphene hybrid nanostructures for enhanced Li-Ion insertion. ACS Nano 3:907–914. https://doi.org/10.1021/nn900150y
37. Bell NJ, Ng YH, Du AJ, Coster H, Smith SC, Amal R (2011) Understanding the enhancement in photoelectrochemical properties of photocatalytically prepared TiO_2-reduced graphene oxide composite. J Phys Chem C 115:6004. https://doi.org/10.1021/jp1113575
38. Huang XD, Zhou XF, Zhou L, Qian K, Wang YH, Liu ZP, Yu CZ (2011) A facile one-step solvothermal synthesis of SnO_2/graphene nanocomposite and its application as an anode material for lithium-Ion batteries. Chem Phys Chem 12:278–281. https://doi.org/10.1002/cphc.201000376
39. Koo HY, Lee HJ, Go HA, Lee YB, Bae TS, Kim JK, Choi WS (2011) Graphene-based multifunctional iron oxide nanosheets with tunable properties. Chem Eur J 17(4):1214–1219. https://doi.org/10.1002/chem.201002252
40. Sundaresan A, Bhargavi R, Rangarajan N, Siddesh U, Rao CNR (2006) Ferromagnetism as a universal feature of nanoparticles of the otherwise nonmagnetic oxides. Phys Rev B 74:161306(R). https://doi.org/10.1103/PhysRevB.74.161306
41. Adineh E, Suli RR (2015) Facile synthesis of decorated graphene oxide sheets with WO_3 nanoparticles. Appl Phys A 120:1587–1592. https://doi.org/10.1007/s00339-015-9359-x
42. Suzuko Y, Toshifumi T, Atsushi Y, Kenzi H (2004) Reaction mechanism of photocatalytic degradation of chlorinated ethylenes on porous TiO_2 pellets: Cl radical-Initiated mechanism. J Phys Chem A 108:5183–5188. https://doi.org/10.1021/jp0311310
43. Javed Q, Wang FP, Rafique MY, Toufiq AM, Li QS, Mahmood H, Khan W (2012) Diameter-controlled synthesis of α- Mn_2O_3 nanorods and nanowires with enhanced surface morphology and optical properties. Nanotechn 23:415603. https://doi.org/10.1088/0957-4484/23/41/415603
44. Lee JW, Hall AS, Kim JD, Mallouk TE (2012) A facile and template-free hydrothermal synthesis of Mn3O4 nanorods on graphene sheets for supercapacitor electrodes with long cycle stability. Chem Mater 24:1158–1164. https://doi.org/10.1021/cm203697w
45. Shen YFR, Zerger P, Deguzman RN, Suib SL, Mccurdy L, Potter DI, O'Young CL (1993) Manganese oxide octahedral molecular sieves: preparation, characterization, and applications. Science 260:511–515. https://doi.org/10.1126/science.260.5107.511
46. Armstrong AR, Bruce PG (1996) Synthesis of layered $LiMnO_2$ as an electrode for rechargeable lithium batteries. Nature 381:499–500. https://doi.org/10.1038/381499a0
47. Giri A, Goswami N, Pal M, Myint MTZ, Al-Harthi S, Singha A, Pal SK (2013) Rational surface modification of Mn_3O_4 nanoparticles to induce multiple photoluminescence and room temperature ferromagnetism. J Mater Chem C 1:1885–1895. https://doi.org/10.1039/C3TC00709J
48. Liu R, Tang H (2000) Oxidative decolorization of direct light red F_3B dye at natural manganese mineral surface. Water Res 34:4029–4035. https://doi.org/10.1016/S0043-1354(00)00166-4
49. Matocha CJ, Sparks DL, Amonette JE, Kukkadapu RK (2001) Kinetics and mechanism of birnessite reduction by catechol. Soil Science Soc Am J 65:58–66. https://doi.org/10.2136/sssaj2001.65158x
50. Petrie RA, Grossl PR, Sims RC (2002) Oxidation of pentachlorophenol in manganese oxide suspensions under controlled

E h and pH environments. Environ Sci Technol 36:3744–3748. https://doi.org/10.1021/es0109491
51. Li H, Lee LS, Schulze DG, Guest C (2003) Role of soil manganese in the oxidation of aromatic amines. Environ Sci Techn 37:2686–2693. https://doi.org/10.1021/es0209518
52. Zhang H, Huang C-H (2005) Oxidative transformation of fluoroquinolone antibacterial agents and structurally related amines by manganese oxide. Environ Sci Techn 39:4474–4483. https://doi.org/10.1021/es048166d
53. Osgouei MS, Khatamian M, Kakili H (2020) Improved visible-light photocatalytic activity of Mn3O4-based nanocomposites in removal of methyl orange. Mater Chem Phys 239:122108. https://doi.org/10.1016/j.matchemphys.2019.122108
54. Mousa MA, Rashad MM Rashad, Mokhtar MM, Mahmoud E. El Shazli (2020) Synthesis, characterization and photocatalytic activity of visible-light-driven Mn_3O_4 and reduced graphene oxide- $M_{n3}O_4$ nanocomposite. J Basic Environ Sci 7: 171–184. Online: 2356-6388
55. Rahaman H, Ghosh SK (2016) Soft-templated synthesis of Mn3O4 microdandelions for the degradation of alizarin red under visible light irradiation. RSC Adv 6(6):4531–4539. https://doi.org/10.1039/c5ra25935e
56. Ghosh S, Basu SM, Baskey (Sen) (2017) Decorating mechanism of Mn_3O_4 nanoparticles on reduced grahene oxide surface through reflux condensation method to improve photcatalytic performance. J Mater Mater Electron 28:17860–17870. https://doi.org/10.1007/s10854-017-7727-3
57. Rizal MY, Saleh R, Prakoso SP, Taufik A, Yin S (2021) Ultraviolet- and visible-light photocatalytic and sonophotocatalytic activities toward Congo red degradation using Ag/Mn3O4 nanocomposites. Mater Sci Semicond Process 121:105371. https://doi.org/10.1016/j.mssp.2020.105371
58. Kefeni KK, Mamba BB (2020) Photocatalytic application of spinel ferrite Nanoparticles and nanocomposites in waste water treatment: Review. Sus Mat Tech 23:e00140. https://doi.org/10.1016/j.susmat.2019.e00140
59. Hu CY, Liu T, Chen F, Zhang R (2013) A brief review of graphene-metal oxide composite synthesis and applications in photocatalysis. J Chin Adv Mat Soc 1(1):21–39. https://doi.org/10.1080/22243682.2013.771917
60. Ma Y, Si C, Yang X, Li J, Wang Z, Shu X, Ye W, Zhou P, Budziangowski WM (2019) Clean synthesis of RGO/Mn_3O_4 nanocomposite with well-dispersed Pd nanoarticle as high-performance catalyst for hydroquinone oxidation. J Col Inter Sci 552:73–83. https://doi.org/10.1016/j.jcis.2019.05.009
61. Li Y, Qu J, Gao F, Lv S, Shi L, He C, Sun J (2015) In situ fabrication of Mn_3O_4 decorated graphene oxide as a synergistic catalyst for degradation of methylene blue. Appl Catal B 162:268–274. https://doi.org/10.1016/j.apcatb.2014.06.058
62. Ahmed AA, Reda SM, Mousa MA, Mohamed MM (2017) Mn_3O_4/graphene nanocomposites: outstanding performances as highly efficient photocatalysts and microwave absorbers. RSC Adv 7:826–839. https://doi.org/10.1039/c6ra24815b
63. Duan L, Wang Z, Hou Y, Wang Z, Gao G, Chen W, Alvarez PJJ (2016) The oxidation capacity of Mn_3O_4 nanoparticles is significantly enhanced by anchoring them onto reduced graphene oxide to facilitate regeneration of surface-associated Mn(III). Water Res 103:101–108. https://doi.org/10.1016/j.watres.2016.07.023
64. Chandra S, Das P, Bag S, Bhar R, Pramanik P (2012) Mn_2O_3 decorated graphene nano-sheet: an advance material for the photo catalytic degrading of organic dynes. Mater Sci Eng 177:855–869. https://doi.org/10.1016/j.mseb.2012.04.006
65. Ullah AKMA, Kibria ASMF, Aktor M, Khan MNI, Tarq ARM, Firoz SH (2017) Oxidative degradation of methylene blue using Mn_3O_4 nanoparticles. Water Conserv Sci Eng 1:249–256. https://doi.org/10.1007/s41101-017-0017-3
66. Robkhob P, Tang IM, Thongmee S (2019) Magnetic properties of the dilute magnetic semiconductor $Zn_{1-x}Co_xO$ nanoparticles. J supercond Nov Magn 32:3637–3645. https://doi.org/10.1007/s10948-019-5135-z]
67. Liua PB, Zhanga YI, Jing YN, Huanga Y, Xiab L, Guang ZX (2019) Synthesis of lightweight N-doped graphene foams with open reticular structure for high-efficiency electromagnetic wave absorption. Chem Eng J 368:285–298. https://doi.org/10.1016/j.cej.2019.02.193
68. Bahramia A, Kazeminezhada I, Abdi Y (2019) Pt-Ni/rGO counter electrode: electrocatalytic activity for dyesensitized solar cell. Superlattices Microstruct 125:125–137. https://doi.org/10.1016/j.spmi.2018.10.026
69. Ban FY, Majid SR, Huang NM, Lim HN (2012) Graphene oxide and its electrochemical performance. Int J Electrochem Sci 7(4345):4351
70. Liu Y, Luo C, Cuia G, Yan SQ (2015) Synthesis of manganese dioxide/iron oxide/graphene oxide magnetic nanocomposites for hexavalent chromium removal. RSC Adv 5:54156. https://doi.org/10.1039/c5ra06455d
71. Yan J, Fan ZJ, Wei T, Qian WZ, Zhang ML, Wei F (2010) Preparation of a graphene nanosheet/polyaniline composite with high specific capacitance. Carbon 48:487–493. https://doi.org/10.1016/j.carbon.2009.09.066
72. Kumar V, Gupta RK, Gundampati RK, Singh DK, Mohan S, Hadi Hasan SH, Malviya M (2018) Enhanced electron transfer mediated detection of hydrogen peroxide using a silver nanoparticle–reduced graphene oxide–polyaniline fabricated electrochemical sensor. RSC Adv 8:619–631. https://doi.org/10.1039/C7RA11466D
73. Yan J, Fan ZG, Wei T, Qian WH, Zhang MI, Wei F (2010) Fast and reversible surface redox reaction of graphene–MnO_2 composites as supercapacitor electrodes. Carbon 48(13):3825–3833. https://doi.org/10.1016/j.carbon.2010.06.047
74. Toufiq AM, Wang FP, Javed QUA, Li QS, Li Y (2014) Hydrothermal synthesis of $Cu0_{.45}Mn0_{.55}O_2$ nanowhiskers: structural characterizations and optical properties. Mater Lett 118:34–38. https://doi.org/10.1016/j.matlet.2013.12.038
75. Song L, Zhang S, Wu X, Wei Q (2012) Controlled synthesis and optical properties of 1D frog egg-like $Mn(IO_3)_2$ /MnO_2 composite nanostructures with ultra-high aspect ratio. Chem Eng J 187:385–390. https://doi.org/10.1016/j.cej.2012.01.131
76. Wi'sniewski K, Zorenko YU, Gorbenko V, Zorenko T, Kukli'nski B, Grinberg M, (2010) High pressure spectroscopy study of SCF Tb3Al5O12 Mn. J Phys Conf Ser 249:012015. https://doi.org/10.1088/1742-6596/249/1/012015
77. Nag A, Cherian R, Mahadevan P, Gopal AV, Hazarika A, Mohan A, Vengurlekar AS, Sarma DD (2010) Size-dependent tuning of Mn^{2+} d emission in Mn^{2+}-doped CdS nanocrystals: bulk vs surface. J Phys Chem C 114:18323–18329. https://doi.org/10.1021/jp105688w
78. Hazarika A, Pandey A, Sarma DD (2014) Rainbow emission from an atomic transition in doped quantum dots. J Phys Chem Lett 5:2208–2213. https://doi.org/10.1021/jz500937x
79. Zhang H, Lv X, Li Y, Wang Y, Li J (2009) P25-Graphene composite as a performance photocatalyst. ACS Nano 4:380–386. https://doi.org/10.1021/nn901221k
80. Patra KK, Ghosalya MK, Bajpaj H, Raj S, Gopinath CS (2019) Oxidative disproportation of MoS2/MoS3-x/RGO multifunctional nanocomposites for solar hydrogen from near-infared to visible region. J Phys Chem C 123:21685–21693. https://doi.org/10.1021/acs.jpcc.9b05983
81. Tudu B, Najajala N, Reddy KP, Saikia P, Gopinath CS (2018) Electronic integration and thin film aspects of Au-Pd/rGO/TiO_2 for

improved solar hydrogen generation. ACS Appl Mater Interfaces 11:32869–32878. https://doi.org/10.1021/acsami.9b07070

82. Bharad PB, Siuaranjani K, Gopinatb CS (2015) A rational approach towards enhancing solar water splitting: A case study of Au-RGO/N-RGO-TiO_2. Nanoscale 7:11286. https://doi.org/10.1039/C5NR02613Jhem. Phys. Chem. 17:1087–1094. https://doi.org/10.1002/cphc.201500953